Journal of Materials Chemistry C

ROYAL SOCIETY OF CHEMISTRY

PAPER

View Article Online
View Journal | View Issue

Cite this: J. Mater. Chem. C, 2020, 8, 11209

Microstructural modulation of organic passivation layers for metal oxide semiconductors to achieve high bias stability†

Dongil Ho,[a] Ha-Yun Jeong,[b] Minh Nhut Le,[c] Hakan Usta,[d] Hyuck-In Kwon,[b] Myung-Gil Kim *[c] and Choongik Kim *[a]

Received 19th May 2020,
Accepted 7th July 2020

DOI: 10.1039/d0tc02393k

rsc.li/materials-c

Electrical properties of metal oxide thin-film transistors (TFTs) are tuned *via* the microstructural control of organic back-channel passivation layers. In this study, organic semiconductor (OSC) passivation layers with various molecular and physicochemical properties are employed to identify the back-channel passivation mechanism in solution-processed amorphous indium gallium zinc oxide (*a*-IGZO) TFTs. The OSC microstructure influences the passivation of electrical defects in *a*-IGZO TFTs by compensating for acceptor-like trap states and dangling bonds in the back-channel. First, the distance between an n-type OSC (C_{60}) and the *a*-IGZO back-channel is controlled by employing phosphonic acid molecules with different carbon chain lengths. Positive bias stress stability is tuned by applying both the OSC and carbon chain effect, leading to stable, high-performance TFTs with the determination of subgap density of states to confirm the compensation effects on the total acceptor-like defect states. The n-doping of identical passivation layers is further investigated by using perylenedicarboximide derivatives to confirm the proposed n-doping mechanism. Finally, the semiconductor 4,4-difluoro-4-bora-3*a*,4*a*-diaza-*s*-indacene is selected on the basis of our proposed passivation model and exhibited good passivation characteristics. This study demonstrates an ideal molecular design for organic passivation layers, which shows significant potential for the realization of stable, high-performance TFTs.

1. Introduction

The vast expansion of the IT industry and the wide use of high-end technologies has given rise to a demand for high-resolution, high-frame-rate displays and the development of flexible and wearable next-generation electronic devices. To meet the high demand for state-of-the-art devices, new semiconductors and innovative processing techniques for thin-film transistors (TFTs), with advantages such as large-area application, high electrical performance, multiple functionalities, and low fabrication cost, have been developed over the last few decades.[1–4] Amorphous oxide semiconductors (AOSs) have attracted much interest as a replacement for conventional silicon-based semiconducting materials owing to their remarkable electrical performance [electron mobility (μ_e) $>$ 10 $cm^2\ V^{-1}\ s^{-1}$ and current on/off ratio (I_{on}/I_{off}) $>$ 10^6] and good electrical uniformity arising from their homogeneous amorphous structure.[5,6] Amorphous indium gallium zinc oxide (*a*-IGZO) obtained using low-cost solution-processing methods at a processing temperature as low as 150 °C exhibits high electrical performance, opening a new avenue to low-cost printable electronics on flexible substrates.[2,7] To date, *a*-IGZO TFTs have been used as switching and driving TFTs for active-matrix liquid crystal displays and organic light-emitting diodes.[8,9] Although these materials exhibit high electron mobility, which decreases the pixel charging time and RC delay in the signal line,[10] stability and reliability issues are the main obstacle to practical applications, where stresses such as voltage bias, illumination, temperature, and ambient effects are critical limitations.[11–14] The degradation of electrical characteristics for the sputtered *a*-IGZO TFTs is known to be originated from the scattering centers, weak oxygen bonds, and ionized oxygen vacancies which are all created due to the high energy of the target ion and Ar^+ incorporation during the sputtering procedure.[15,16] Therefore, to stabilize the channel layer of sputtered a-IGZO TFTs, activation process which utilize thermal energy is required,[17] and researchers have succeeded in

[a] Department of Chemical and Biomolecular Engineering, Sogang University, 1 Shinsoo-dong, Mapo-gu, Seoul 04107, Republic of Korea. E-mail: choongik@sogang.ac.kr
[b] School of Electrical and Electronics Engineering, Chung-Ang University, 84 Heukseok-ro, Dongjak-gu, Seoul 06974, Republic of Korea
[c] School of Advanced Materials Science and Engineering, Sungkyunkwan University, Suwon 16419, Republic of Korea. E-mail: myunggil@skku.edu
[d] Department of Materials Science and Nanotechnology Engineering, Abdullah Gul University, Kayseri 38080, Turkey

† Electronic supplementary information (ESI) available. See DOI: 10.1039/d0tc02393k

commercialization *via* activation temperatures above 300 °C. Compared to the commercialized sputtered *a*-IGZO, solution-processed *a*-IGZO exhibit inferior stability due to the chemical reactions of the precursors during the sol–gel process.[18] Intensive investigations have been conducted to enhance the performance and stability of solution-processed *a*-IGZO up to the sputtered level, but still there were limitations. Defect states were difficult to remove for low temperature processes which are required for the realization of next-generation flexible/stretchable devices. In particular, the stability of AOS TFTs against voltage bias stress is crucial, because the on/off states of TFTs are determined by the voltage biases, making bias stress unavoidable in practical applications. For n-type metal oxide semiconductors, positive bias stress (PBS) has been extensively studied to understand the contribution of electron traps and acceptor-like states in the channel to the positive shift in the threshold voltage.[19] Amorphous structural and electronic defects such as oxygen or metal ion vacancies, substitutions, anti-site defects, interstitial atoms, and dangling bonds are known to form additional electronic defect states in the band gap of AOSs and act as carrier traps.[20–23] In addition, most metal oxide TFTs are sensitive to extrinsic impurities such as oxygen and water molecules, which are absorbed through the semiconductor back-channel surface and then capture electrons from the conduction band, creating a depletion region in the back channel.[24–26] These factors together result in poor stability and large hysteresis in the current–voltage performance of the devices.[24–26] Therefore, it is essential to compensate for the defect states and block ambient impurities in order to realize high-stability devices.

To address these issues, the deposition of additional passivation layers on the back channel of the AOS surface has been intensively studied. Various compounds such as SiO_x, MgF_2, Al_2O_3, TiO_x, and Y_2O_3 have typically been employed as inorganic materials for the passivation layer.[10,14,27–30] However, most of these materials require a high fabrication temperature and a costly vacuum deposition process, and therefore hinder application to flexible substrates. Furthermore, the plasma-based vacuum process causes additional device degradation such as negative threshold voltage shifts and large off-currents.[31,32] By contrast, organic materials used as passivation layers are generally fabricated by a solution process, so the disadvantages of the vacuum-based fabrication methods used for inorganic materials may be avoided. Conventional organic materials used for passivation include monolayers of phosphonic acids,[33,34] alkoxysilanes, and alkanethiols,[35] and polymers such as poly(methyl methacrylate),[36,37] CYTOP,[38] polydimethylsiloxane,[39] and SU-8 resist.[40] Recent studies demonstrated that nitrocellulose[41] or instant glue[42] on the back channel of IGZO TFTs could modify the chemical stoichiometry of the IGZO films and block the adsorption of moisture and oxygen. In addition, we have investigated phenyl-C61-butyric acid methyl ester (PCBM) fullerene derivatives for use as solution-processed interfacial layers between copper electrodes and an IGZO semiconducting layer, where the organic layer not only passivated the IGZO back channel, but also prevented copper ion migration from the electrodes to the semiconducting layer.[43] Previous studies also reported successful application of organic materials as passivation layers on the back channel of oxide semiconductors *via* a simple immersion or spin-coating process and demonstrated improved device stability.[44] However, most studies have not described the detailed passivation mechanisms or how to control and modify the passivation effect. To further expand the use of organic materials for efficient passivation, and hence to obtain stable, high-performance devices for state-of-the-art electronics, in-depth study that establishes an ideal model of organic passivation is crucial.

In this study, the physicochemical characteristics of organic semiconducting materials for passivation layer application were carefully controlled and analyzed to clarify the dominant properties that affect the back-channel passivation capability. Because most organic semiconductor (OSC) structures consist of a π-conjugated core with alkyl chain substituents, we designed an organic passivation model in which alkyl chains are used to separate the π-conjugated core from the back channel. Alkyl chain substitutions play a key role in 3D charge transfer in a molecular design for OSCs.[45,46] These chains produce distinctive molecular stacking structures; hence, the charge transfer characteristics depend on the stacking direction.[47,48] Alkyl chains are also considered as insulating materials, where vertical charge transfer is affected by the chain length in edge-on stacking structures.[49–51] Therefore, a detailed investigation of the effect of the molecular behavior on organic back-channel passivation will provide insight into molecular engineering of organic passivation materials. Phosphonic acid (PA) molecules with alkyl chain lengths of 8, 12, and 18 were applied in solution-processed *a*-IGZO semiconductors with an SiO_2 dielectric to vary the distance between the back channel of the *a*-IGZO and the C_{60} fullerene n-type OSCs, which were deposited on the PA-modified *a*-IGZO to obtain ideal isotropic charge transfer. Detailed X-ray photoelectron spectroscopy (XPS) analysis revealed that back-channel passivation compensated for a significant number of oxygen vacancies and subsequent hydroxide generation, reducing the positive shifts in the threshold voltage (ΔV_{th}) during PBS tests for up to 3600 s. For the unpassivated *a*-IGZO and C_{60}-passivated devices with alkyl chain lengths of 0 (no PA treatment), 8, 12, and 18, the ΔV_{th} values were 34, 21, 13, 4, and 11 V, respectively. As the PA alkyl chain length increased from 0 to 18, not only was the passivation effect of the OSC (C_{60}) minimized owing to the increased distance from the back channel, but also the passivation effect of the alkyl chains was maximized. The optimal ΔV_{th} value of 4 V was obtained at an alkyl chain length of 12. This result reveals that the overall organic passivation capability originates from the combined effect of the OSC and the alkyl chain. Furthermore, stable, high-performance devices were realized by applying the optimal passivation conditions, and the density of states (DOS) in devices with and without the passivation layers was determined. To this end, the n-doping characteristics of the organic passivation layer were investigated using the same passivation model. The results were verified by employing n-type perylenedicarboximide (PTCDI) derivatives with chain lengths of 1, 8, 13, and 18 as passivation layers, where the n-doping behavior corresponded well with that of the proposed

model. A detailed understanding of organic back-channel passivation of *a*-IGZO oxide semiconductors would provide efficient design strategies for organic passivation materials and allow the further development of highly stable high-performance AOS TFTs for application in state-of-the-art devices.

2. Results and discussion

The schematic in Fig. 1a shows the effect of the organic passivation layer on the *a*-IGZO TFTs. Organic molecules on the back channel of metal oxide semiconductors can compensate for electronic defects such as oxygen or metal ion vacancies, substitutions, anti-site defects, interstitial atoms, and dangling bonds, which may act as carrier traps, thus affecting the DOS in the band gap.[52–54] The addition of organic materials to the back channel of metal oxide semiconductors can reportedly passivate electron trap sites.[41,42,55] In unpassivated TFT devices based on metal oxide semiconductors, defect states in the active layer generally induced electron traps and a corresponding positive shift in the threshold voltage during PBS tests.

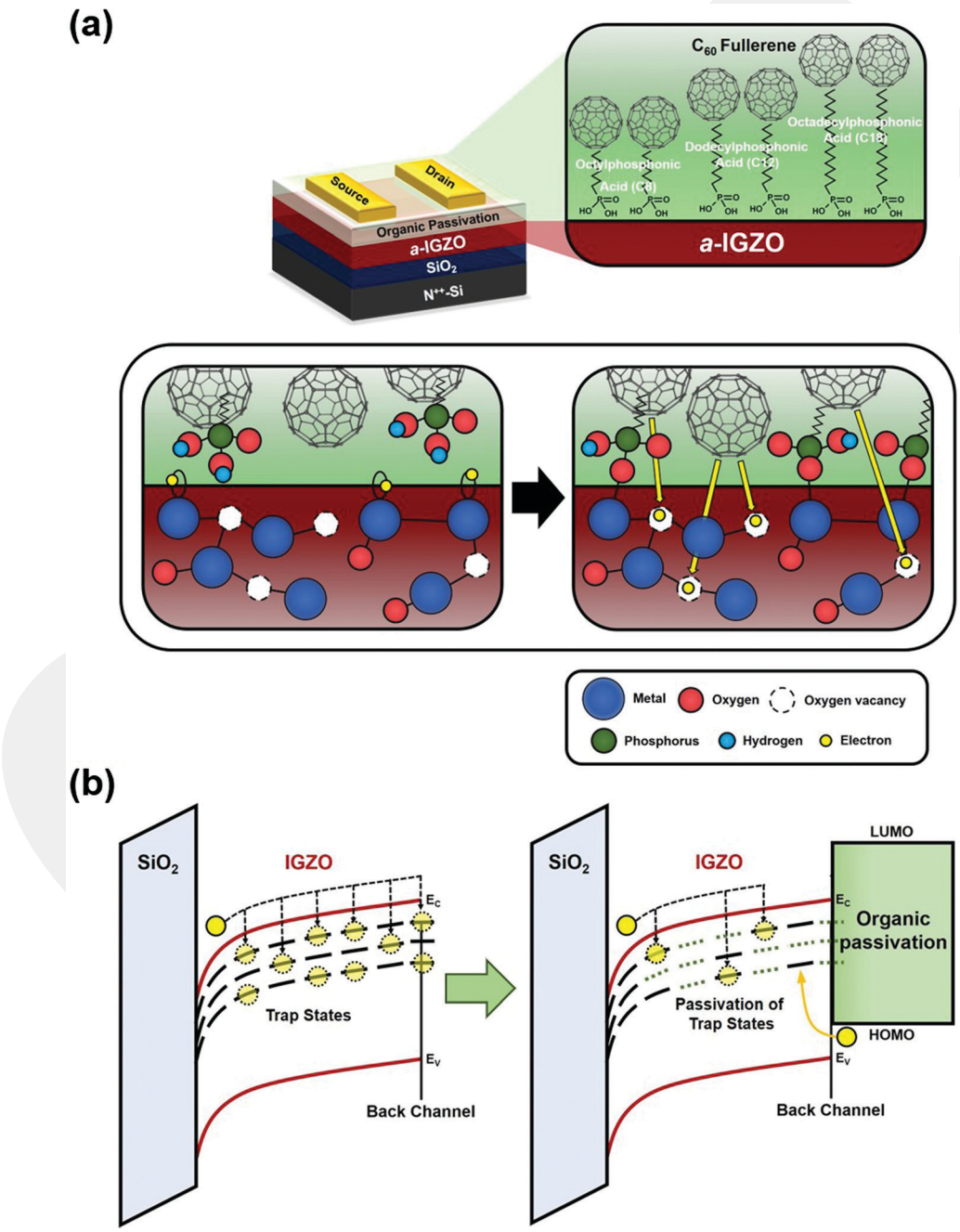

Fig. 1 (a) Schematic showing effect of organic passivation on the *a*-IGZO back channel employed in this study and (b) energy band diagram of unpassivated and passivated *a*-IGZO TFTs, which illustrates the passivation mechanism.

This paper proposes a mechanism for organic back-channel passivation (Fig. 1a) and establishes a model system for the design of organic passivation molecules. The spherical OSC C_{60} was applied as the organic passivation layer. C_{60} fullerenes are one of the most widely used n-type component in organic TFTs and photovoltaics. Due to their low lowest unoccupied molecular orbital (LUMO) levels and ionization energies that are near the metal oxide work function, sufficient electron transfer from the OSCs to *a*-IGZO is expected.[43] Since we have explored fullerene-based materials as a potential back-channel passivation material in our previous study,[43] C_{60} fullerenes were selected as OSCs for passivation in which the filling of subgap states is anticipated. Moreover, owing to the spherical shape of C_{60}, convenient tuning of the distance between the passivation layer and the back channel is possible, enabling efficient charge transfer by the organic passivation molecules. To investigate the effects of passivation, an organic layer was employed on solution-processed *a*-IGZO. To clearly identify these effects, *a*-IGZO was fabricated by a sol–gel processing method and annealed at 310 °C to create unstable devices. To tune the distance between C_{60} and the back channel, PA monolayers with alkyl chain lengths of 8, 12, and 18 were deposited on top of the *a*-IGZO back channels. Analysis of the threshold voltage and on-voltage shifts during PBS tests suggests that the passivation effect is determined by the combined effect of the OSC and the alkyl chain. Furthermore, use of the optimal passivation conditions resulted in minimal threshold voltage shifts against the PBS and a corresponding reduction in the DOS trap states. Hence, effective suppression of defect and trap states in the back channel and semiconductor layer is crucial to achieving stable device operation of metal oxide semiconductor TFTs (Fig. 1b). Note that, the ambient instability of organic n-channel devices does not apply in this study, since such instability will occur when the organic semiconductor is employed as the channel layer. Organic materials which are employed here are utilized as passivation layers on top of a-IGZO which provides the actual n-channel for the TFT device. Considering the lack of electron accumulation, these organic semiconductors only act as electron-donating defect-passivation materials.

2.1 Microstructural and chemical changes in *a*-IGZO films after organic passivation

To investigate the microstructural and chemical changes in the *a*-IGZO films due to the control of organic passivation, we characterized the as-prepared and passivated *a*-IGZO films using atomic force microscopy (AFM), X-ray diffraction (XRD), and XPS. The thin (15 nm) *a*-IGZO films (Fig. S1a and b in the ESI†) derived from a soluble precursor, as well as the *a*-IGZO films with PA-treatment (Fig. S1c–g, ESI†) did not show any crystalline diffraction peaks, indicating amorphous structure. The thin films of vacuum-deposited C_{60}, which were employed as the outermost part of the organic passivation layer, also exhibited no XRD diffraction peaks, demonstrating their amorphous nature (Fig. S1h–k, ESI†).[56] The AFM images in Fig. S2 (ESI†) show that the *a*-IGZO, *a*-IGZO/C_8 PA, *a*-IGZO/C_{12} PA, and *a*-IGZO/C_{18} PA films have smooth surface morphologies, with root-mean-square (RMS) roughness values of 0.32, 0.36, 0.29, and 0.31 nm, respectively. The 30 nm-thick C_{60} films exhibit island-like morphologies, with an RMS roughness of 4.4–5.1 nm. Additionally, to confirm the proper placement of the PA monolayers on the back channel of the *a*-IGZO films, the contact angles of the film surface were measured (Fig. 2). Aqueous contact angles of 74.6°, 103.9°, 109.5°, and 112.1° were observed for the *a*-IGZO, *a*-IGZO/C_8 PA, *a*-IGZO/C_{12} PA, and *a*-IGZO/C_{18} PA films, respectively. The higher contact angles for the PA-treated *a*-IGZO films indicate hydrophobic surface characteristics resulting from the carbon chains of the PA monolayers.[57] Because the deposition of an organic passivation layer on AOSs is a nondestructive process, the microstructural and morphological analyses using XRD and AFM showed no disruption of the atomic order and indicated proper fabrication of the passivation layer on the *a*-IGZO films. Further spectroscopic analysis was employed to investigate the local changes in the chemical bonds.

XPS was used to investigate the local chemical environment of the metal oxide semiconductor and the changes in the *a*-IGZO TFT back channel chemistry after the PA monolayers and C_{60} were applied as passivation layers. To exclude unwanted reactions or additional oxygen vacancy formation, the surfaces of the thin films were not etched further.[58] In the O 1*s* spectrum of the *a*-IGZO film (Fig. 2a and b), three peak components at low (~530 eV), intermediate (~531 eV), and high binding energy (~532 eV) could be assigned to the M–O–M lattice oxygen, M–O_{vac}–M oxygen vacancy, and M–OH hydroxide, respectively.[7,59] PA-treated *a*-IGZO (*a*-IGZO/C_8 PA, *a*-IGZO/C_{12} PA, and *a*-IGZO/C_{18} PA) showed the main O 1*s* peak at 530.5 eV (full width at half-maximum, 2.8 eV) originating from the *a*-IGZO lattice.[61] Among the three peak components, the O 1*s* component at intermediate binding energy can be attributed to P–O–M (P–O–In/P–O–Ga/P–O–Zn) and P=O, in agreement with previous studies.[60–62] It is known that surface hydroxyl groups are replaced with P–O–M bonds,[63] and, as shown in Fig. 2, the decrease in the M–OH hydroxide peak corresponds to the increase in the P–O–M peak when PA monolayers with longer alkyl chains are used, indicating densely ordered monolayers on the *a*-IGZO back channel. Additionally, the intensity ratio of the intermediate- and low-binding-energy peaks ($I_{intermed}/I_{low}$) provides a qualitative estimate of the relative number of ordered monolayer on the surface.[64] As shown in Fig. 2f, the $I_{intermed}/I_{low}$ ratio is 74%, 89%, and 94% for the *a*-IGZO/C_8 PA, *a*-IGZO/C_{12} PA, and *a*-IGZO/C_{18} PA films, respectively; this results suggests better molecular packing and subsequent formation of high-density PA monolayers with longer alkyl chains.

The O 1*s* XPS spectra of the films with a C_{60} layer reveal a high-intensity component at 532 eV and an additional peak at 533 eV (Fig. S3, ESI†). The values are in agreement with prior studies in which the peak signal was attributed to the amorphous region of the sample, not to the fullerene bulk.[65] It has also been reported that the low-binding-energy peak corresponds to either hydroxyl- or ether-bonded oxygen in the sample, whereas the high-binding-energy peak can be assigned to surface or subsurface water, which is resistant to evaporation even under vacuum.[66] Because the samples were not in contact with water,

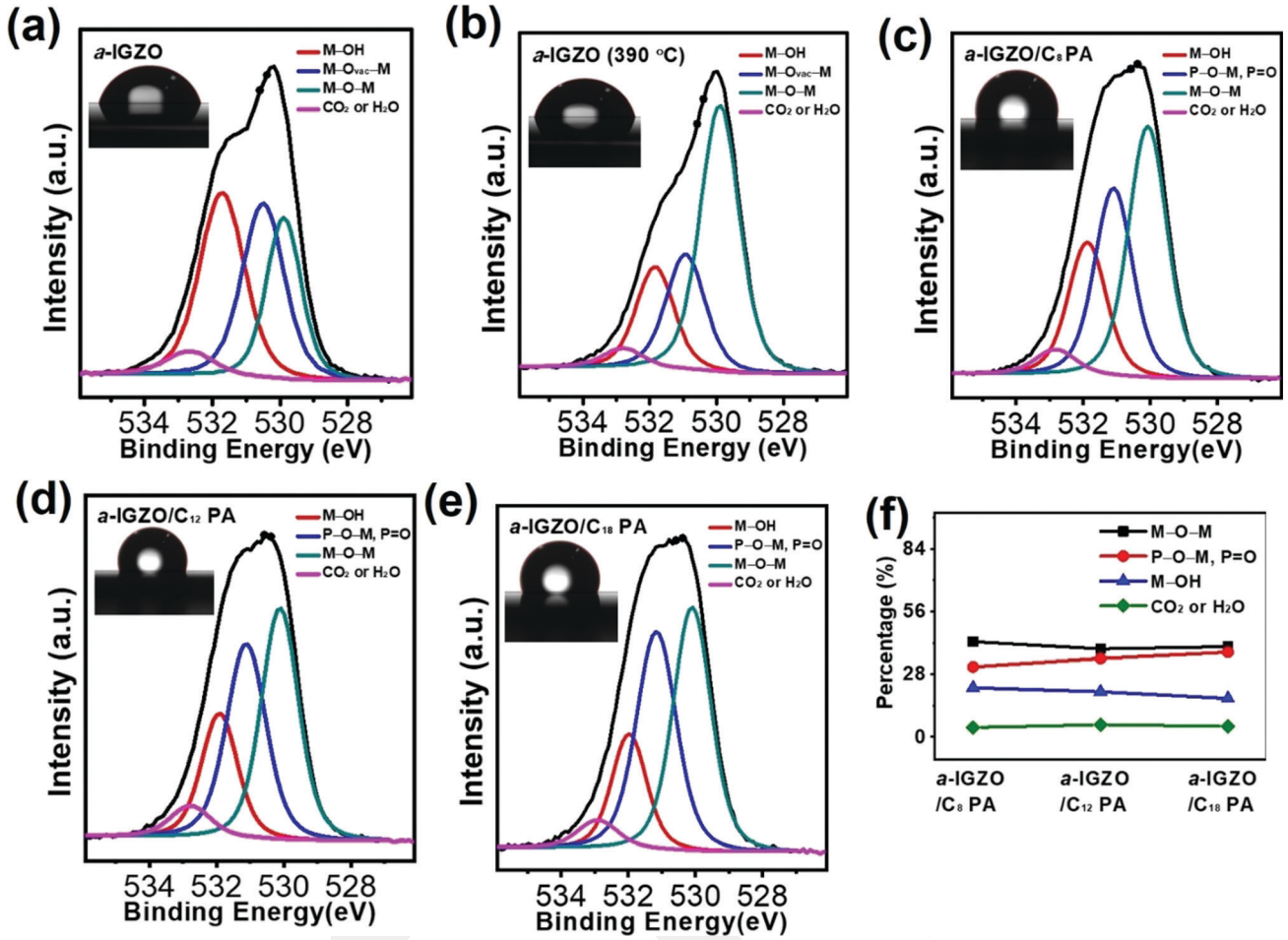

Fig. 2 O 1*s* XPS spectra of (a) *a*-IGZO, (b) *a*-IGZO (390 °C), (c) *a*-IGZO/C_8 PA, (d) *a*-IGZO/C_{12} PA, (e) *a*-IGZO/C_{18} PA with insets of contact angle images, and (f) areal ratio of the M–O–M, P–O–M (and P=O), and M–OH bonding states as determined by XPS O 1*s* analysis of *a*-IGZO/C_8 PA, *a*-IGZO/C_{12} PA, and *a*-IGZO/C_{18} PA films.

absorption from the humid air of the laboratory is thought to have occurred over time. The hydroxyl signals could also result from hydroxyl radical creation by ambient UV light exposure of C_{60} in the presence of water.[67]

2.2 Tuning device stability and density of states *via* organic passivation

PBS tests of top-contact/bottom-gate devices with a thermally grown SiO_2 dielectric (Fig. 1a) were conducted to investigate the tuning of organic passivation effects on the electrical performance and device stability of the *a*-IGZO TFTs. Positive biases of V_G = 70 V and V_{DS} = 30 V were applied for up to 3600 s to observe the positive shifts in the transfer curves. Positive displacement of the threshold voltage (V_{th}) results from trapping of negative charges at the channel/dielectric interface[68,69] or the bulk channel layer (channel defects)[70] during PBS. Consequently, a larger positive gate voltage is required for the device to turn on and reach saturation.[71] Electronic defect states are compensated for by applying organic materials as back-channel passivation layers in *a*-IGZO TFTs, resulting in smaller PBS shifts. The PBS shift of organic passivation materials with different physicochemical characteristics will be observed to establish an organic passivation tuning model of *a*-IGZO TFTs. Note that, the devices were measured in vacuum conditions to exclude the effect of ambient molecule adsorption and desorption, and to focus on the electrical perspective of the passivation layers along with the study of intrinsic defect states of oxide semiconductors.

For this investigation, solution-processed *a*-IGZO thin films annealed at 310 °C were employed as the template for organic passivation. The annealing temperature of the metal oxide film is critical to the condensation reaction and structural relaxation, which removes chemical impurities/byproducts, densifies the film, and reduces the defect states for the sol–gel metal oxide chemical process.[72] Varying the annealing temperature of the *a*-IGZO thin films contributes to changes in the TFT characteristics;[73] an annealing temperature of 310 °C was adopted in this study to produce sufficient defect states for effective observation of the passivation effects. The TFT with an unpassivated *a*-IGZO thin film annealed at 310 °C, which is considered as the reference, exhibits V_{th} shifts of up to 40 V during 3600 s of PBS, as shown in Fig. 3a, b and Fig. S4a (ESI†). For both the unpassivated and passivated devices, typical instability indicators such as rigid positive transfer curve shifts, continuous I_{DS} reduction,

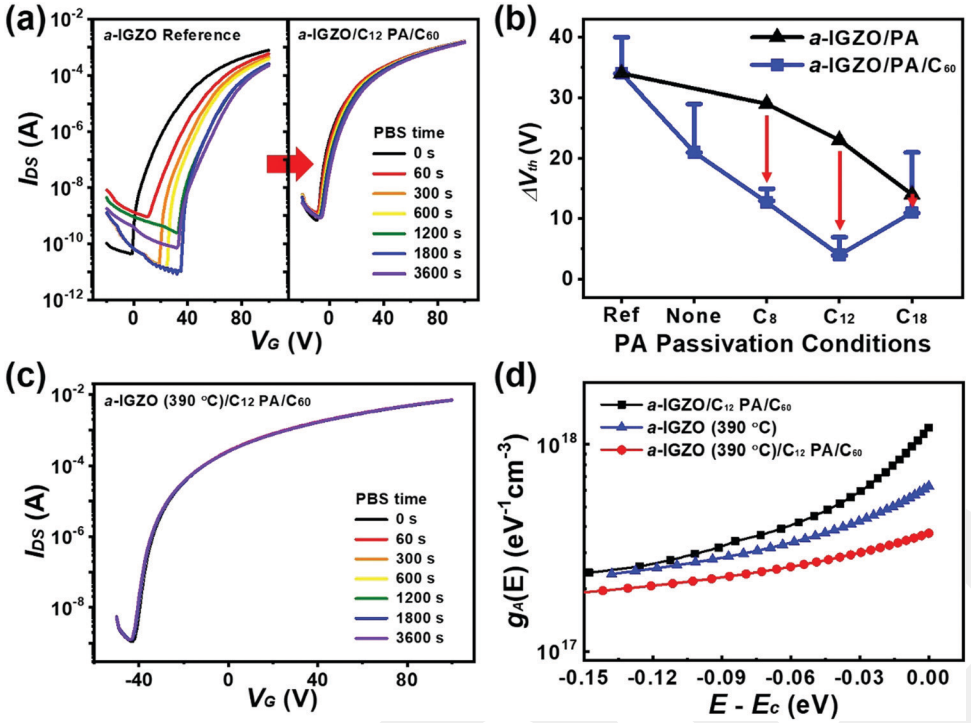

Fig. 3 (a) PBS stability tuning *via* control of organic passivation microstructure, (b) changes in ΔV_{th} of *a*-IGZO/PA and *a*-IGZO/C_n PA/C_{60} with the ΔV_{th} range for multiple devices, (c) PBS test results of *a*-IGZO (390 °C)/C_{12} PA/C_{60}, and (d) the extracted subgap states $g_A(E)$ using the unified subthreshold coupling factor technique for three devices obtained under different fabrication/passivation conditions.

and clockwise hysteresis in the transfer curves were observed throughout the PBS. These behaviors correspond to degradation *via* deep state creation and electron trapping in the *a*-IGZO channel layer, as illustrated in Fig. 1b.[54]

To control the microstructure of C_{60} passivation layers and tune the PBS stability of the TFT devices, PA monolayers were inserted between the *a*-IGZO back-channel and C_{60} passivation layer. In regard of distinguishing the C_{60} passivation effect from the combined effect with PA monolayers, first, PA-treated *a*-IGZO TFTs (*a*-IGZO/C_n PA) were tested. As shown in Fig. 3b and Table 1, the threshold voltage shift (ΔV_{th}) during 3600 s of PBS decreased from 34 V (*a*-IGZO reference) to 29, 23, and 14 V for the *a*-IGZO with PA monolayers with carbon chain lengths of 8, 12, and 18, respectively. It is known that monolayers with alkyl chains longer than 10 carbon atoms show strong cohesive forces; thus, the molecules have an almost upright configuration, resulting in a smooth, well-ordered monolayer.[57] Therefore, electronic degradation resulting from the contribution of dangling bonds at the *a*-IGZO back channel[16,74,75] would be compensated by phosphate groups with longer alkyl chains, resulting in enhanced stability during PBS tests. PAs are known to show strong binding affinity to metal oxides, resulting in strong covalent P–O–M anchoring.[76,77] Furthermore, PA adsorption on the *a*-IGZO back channel can also eliminate the dangling bonds of the metal cations by forming chained phosphate groups.[78–80] Because dangling bonds or under-coordinated cations form localized defect states near the conduction band minimum (CBM), acting as electron traps and inducing threshold instability,[81] organic passivation of such defect states results in stable device performance, which is consistent with the O 1*s* XPS spectra in Fig. 2.

Next, the microstructure-controlled C_{60} passivation devices (*a*-IGZO/C_n PA/C_{60}) were examined. The distance between the *a*-IGZO and the C_{60} organic layer increases gradually as the chain length of the PA increases from 0 (reference) to 8, 12, and 18. In PBS tests of the representative device *a*-IGZO/PA/C_{60} (Fig. 3a and Fig. S4, ESI†), ΔV_{th} values of 21, 13, 4, and 11 V were observed for the unpassivated and C_8-, C_{12}-, and C_{18}-PA passivated devices, respectively. Additional ΔV_{th} reductions (indicated by red arrows in Fig. 3b) of 13, 16, and 19 V were observed for *a*-IGZO/none/C_{60}, *a*-IGZO/C_8 PA/C_{60}, and *a*-IGZO/C_{12} PA/C_{60}, respectively, compared with the reference and *a*-IGZO/C_n PA devices, indicating optimal passivation in the *a*-IGZO/C_{12} PA/C_{60} device. On the other hand, an additional ΔV_{th} reduction of only 3 V was observed for the *a*-IGZO/C_{18} PA/C_{60} device, indicating that the passivation strength of the C_{60} was reduced owing to the distance of the layer from the back channel. The passivation effect can be confirmed by investigating multiple devices, and the ΔV_{th} range is presented in Fig. 3b. Because *a*-IGZO contains subgap defect states within ~2 nm of the film surface,[82] fullerene derivatives can be regarded as electron-donating defect-passivation materials when deposited on the back-channel surface, with an effect similar to the reported *a*-IGZO back-channel passivation by Y_2O_3 metal oxide materials.[83] Therefore, the primary reason for the improved PBS stability arises from the compensation of subgap defect states in the semiconductor layer, which can be controlled

Table 1 Representative electrical performance of *a*-IGZO TFTs passivated by various phosphonic acid (PA) monolayers and C_{60}.[a] [μ_e: electron mobility ($cm^2\ V^{-1}\ s^{-1}$), V_{th}: threshold voltage (V), I_{on}/I_{off}: current on/off ratio]

			Positive bias stress (s)							
PA	Org. pass.	Parameter	0	60	300	600	1200	1800	3600	Δ
None	None	μ_e	1.6	1.6	1.6	1.6	1.6	1.5	1.6	0
		V_{th}	31	44	47	52	61	60	65	34
		I_{on}/I_{off}	1.8×10^7	1.1×10^7	3.3×10^7	3.2×10^7	2.4×10^6	3.0×10^7	4.6×10^6	
None	C_{60}	μ_e	1.7	1.8	1.8	2.0	2.1	2.5	2.6	0.9
		V_{th}	8.4	13	18	20	25	26	29	21
		I_{on}/I_{off}	2.1×10^6	1.3×10^6	1.0×10^6	1.3×10^6	2.4×10^6	3.4×10^6	4.7×10^6	
C_8	None	μ_e	1.4	1.5	1.6	1.6	1.6	1.6	1.6	0.2
		V_{th}	10	20	25	29	33	35	39	29
		I_{on}/I_{off}	3.6×10^6	2.0×10^6	2.7×10^6	2.2×10^6	6.3×10^6	7.7×10^6	9.2×10^6	
C_8	C_{60}	μ_e	2.1	2.0	2.0	2.0	2.1	2.3	2.4	0.3
		V_{th}	6.3	8.3	11	13	15	16	19	13
		I_{on}/I_{off}	1.7×10^6	1.3×10^5	2.7×10^5	3.5×10^5	5.1×10^5	6.6×10^5	9.4×10^5	
C_{12}	None	μ_e	1.6	1.8	1.8	1.9	1.9	1.9	1.9	0.3
		V_{th}	8.7	14	19	23	26	29	32	23
		I_{on}/I_{off}	9.9×10^6	6.8×10^6	7.7×10^6	7.8×10^6	7.3×10^6	7.5×10^6	7.8×10^6	
C_{12}	C_{60}	μ_e	1.8	1.9	2.0	2.0	2.0	2.0	2.1	0.3
		V_{th}	12	12	13	15	16	16	16	4
		I_{on}/I_{off}	3.0×10^6	1.4×10^6	2.0×10^6	2.3×10^6	2.5×10^6	2.5×10^6	2.5×10^6	
C_{18}	None	μ_e	2.1	2.3	2.3	2.3	2.4	2.4	2.2	0.1
		V_{th}	9.8	13	16	19	20	22	24	14
		I_{on}/I_{off}	4.7×10^6	3.4×10^6	3.6×10^6	3.9×10^6	3.8×10^6	3.6×10^6	4.2×10^6	
C_{18}	C_{60}	μ_e	2.2	2.2	2.3	2.3	2.3	2.3	2.4	0.2
		V_{th}	14	16	18	19	20	21	25	11
		I_{on}/I_{off}	3.0×10^6	2.8×10^6	2.7×10^6	2.6×10^6	2.4×10^6	2.5×10^6	2.4×10^6	

[a] Measured in vacuum; exhibited n-type characteristics.

by structural modification of the passivation material. The ΔV_{th} results illustrate that the electron-donating defect-passivation effect is hindered when the distance between the back-channel surface and the passivation molecule exceeds a chain length of 12. This indicates that alkyl chain length modification of the organic molecules is critical to organic passivation effects and can be further proposed as a molecular design strategy for organic passivation materials. The DOS measurement will be further discussed in the following sections.

Stable high-performance devices were realized by applying the optimal passivation conditions to TFTs made with *a*-IGZO annealed at 390 °C. Because of the high annealing temperature, the unpassivated *a*-IGZO (390 °C) TFT exhibits a ΔV_{th} value of 2 V, as shown in Fig. S4f (ESI†) and Table 2. This stability arises from the decrease in oxygen vacancies (Fig. 2b), which are known to remain as deep traps in the active layer or to generate hydroxides by absorption of water into the vacancies.[84] By applying the optimal passivation by C_{12} PA/C_{60}, the *a*-IGZO (390 °C)/C_{12} PA/C_{60} device exhibited a highly stable ΔV_{th} of 0 V and a high electron mobility of 5.4 $cm^2\ V^{-1}\ s^{-1}$ (Fig. 3c). Device stability was also secured for the passivated TFTs when measured in ambient conditions (Fig. S5, ESI†). These results demonstrate the feasibility of a stable, high-performance solution-processed metal oxide thin-film technology obtained by organic back-channel passivation. Furthermore, the devices annealed at 390 °C were employed for DOS measurement to determine the localized states in the band gap and specify their role in organic passivation.

To determine the underlying spectral density of localized states in the band gap, TFTs can be employed to clarify the trap densities as a function of energy, known as the trap DOSs.[85] Because DOSs are regarded as important parameters for determining the electrical characteristics and long-term reliability of devices, DOS analysis of the interface and bulk traps is useful

Table 2 Representative electrical performance of amorphous IGZO thin-film transistors annealed at 390 °C under different C_{60} passivation conditions.[a] [μ_e: electron mobility ($cm^2\ V^{-1}\ s^{-1}$), V_{th}: threshold voltage (V), I_{on}/I_{off}: current on/off ratio]

			Positive bias stress							
PA	Org. pass.	Parameter	0	60	300	600	1200	1800	3600	Δ
None	None	μ_e	4.8	5.0	5.1	5.2	5.2	5.2	5.2	0.4
		V_{th}	9.0	9.4	9.6	10	10	11	11	2.0
		I_{on}/I_{off}	5.9×10^7	4.9×10^7	5.0×10^7	5.1×10^7	5.1×10^7	5.1×10^7	4.9×10^7	
C_{12}	C_{60}	μ_e	5.4	5.5	5.6	5.5	5.2	5.0	5.7	0.3
		V_{th}	−15	−15	−16	−16	−16	−15	−15	0
		I_{on}/I_{off}	5.8×10^6	5.6×10^6	5.4×10^6	5.4×10^6	5.5×10^6	5.6×10^6	5.7×10^6	

[a] Measured in vacuum; exhibited n-type characteristics.

for investigating the device performance of metal oxide semiconductor devices. Oxide semiconductors are known to be composed of donor and acceptor-like DOSs at different positions of the energy band,[19] and theoretical calculations play a major role in identifying the location and the effects of deep or shallow defect states of the oxides.[86,87] For solution-processed oxides, these defects are particularly relevant. Since, metal nitrate hydrates are one of the most widely used precursors in which thermal annealing is the process of eliminating impurities *via* densification, there is a high probability for the presence of oxygen interstitials, hydrogen, or oxygen vacancies, as well as nitrogen defects and other deep states.[18] In particular, DOS measurement can be used to differentiate the mechanisms of PBS instability to reveal the contribution of each mechanism.[19] In addition, several measurement methods have been proposed to model the DOSs and detect the trap densities of both vacuum-processed[53,88–90] and solution-processed metal oxide TFTs.[91,92] Previous studies report detailed analysis on oxide defect states *via* the extraction of subgap DOS ($g_A(E)$) by employing various methods such as *C–V* characteristics,[53,88] photo-induced V_{th} shifts under various wavelengths,[93] the Meyer–Neldel rule of the activation energy,[89] and fitting based on numerical simulation.[94] To investigate the effect of organic passivation on ΔV_{th} in more detail, we experimentally determined the subgap DOSs of the unpassivated and passivated *a*-IGZO TFTs.[95] Notable differences were observed among the *a*-IGZO (310 °C)/C_{12} PA/C_{60}, *a*-IGZO (390 °C), and *a*-IGZO (390 °C)/C_{12} PA/C_{60} devices; these differences were consistent with the PBS results. Fig. 3d shows the DOSs of the three devices fabricated under different conditions. The total DOS decreased in the order *a*-IGZO/C_{12} PA/C_{60} device > *a*-IGZO (390 °C) device > *a*-IGZO (390 °C)/C_{12} PA/C_{60}, which corresponds to the ΔV_{th} results of 4, 2, and 0 V, respectively. Because *a*-IGZO operates in n-channel mode, the DOSs can be considered as acceptor-like states,[94] and the total DOS value near the CBM can be considered to be the summation of the interfacial trap density and the traps in the channel layer. When the devices are passivated, electrons from the highest occupied molecular orbital (HOMO) of the organic passivation layer might be responsible for filling the density of acceptor states below the CBM, which could act as electron traps if they remain unpassivated and vacant. Such acceptor states with a relatively low DOS ($\sim 10^{16}$–10^{17} cm^{-3} eV^{-1}) have been reported *via* device simulations at ~0.8 eV below the CBM.[96] In the presence of organic passivation layers, these acceptor states may be compensated and thus will not act as electron trap sites. Note that it was difficult to determine the DOSs of the reference device, *a*-IGZO (310 °C), because of its unstable electrical performance, which was unsuitable for accurate measurement. Additional organic passivation of *a*-IGZO allowed for proper DOS measurement.

2.3 Doping level control *via* organic passivation

To more closely examine the passivation effect of the organic material, we focused on doping-level control of the oxide semiconductors by organic passivation. Doping-level control contributes to the realization of effective turn-on voltage tuning for oxide semiconductors. However, the electronic properties of AOSs are weakly modified by conventional doping methods owing to the lack of structural ordering in amorphous materials, which hinders the implementation of typical substitutional doping.[97] Therefore, investigation of a nondeforming method of controlling the electrical properties of oxide TFTs has attracted attention to the use of organic materials. For instance, researchers have studied the interface between crystalline oxide semiconductors and organic materials to investigate the charge-transfer doping and band alignment.[98,99] To control the electrical properties of AOSs, charge transfer at the organic–inorganic heterojunction to obtain efficient charge collection or insertion into the organic layer has been thoroughly studied.[100,101] N-Doping of OSCs was employed to tune the electrical properties of *a*-IGZO and well-known n-type OSCs such as PCBM, poly{[*N*,*N*′-bis(2-octyldodecyl)-naphthalene-1,4,5,8-bis(dicarboximide)-2,6-diyl]-*alt*-5,5′-(2,2′-bithiophene)} and 4-(2,3-dihydro-1,3-dimethyl-1*H*-benzimidazol-2-yl)-*N*,*N*-dimethylbenzenamine with low LUMO levels, enabling electron transfer from the OSCs to *a*-IGZO.[39] The use of fullerene derivatives was also reported for bulk charge-transfer doping of solution-processable amorphous metal oxides.[102] However, in-depth study of the effect of the molecular characteristics on organic charge-transfer doping is crucial for the application of organic passivation and/or doping materials.

In this study, the carbon chain length was modified using phosphonic acid monolayers with different chain lengths to control the distance between the *a*-IGZO back channel and C_{60} organic passivation material; as a result, the n-doping characteristics differed. As shown in Table 1, the initial (0 s of PBS) V_{th} values of the *a*-IGZO, *a*-IGZO/none/C_{60}, *a*-IGZO/C_8 PA/C_{60}, *a*-IGZO/C_{12} PA/C_{60}, and *a*-IGZO/C_{18} PA/C_{60} films were 31, 8.4, 6.3, 12, and 14 V, respectively. By positioning the organic passivation material near the back channel, stronger n-doping characteristics could be obtained. Effective charge transfer can occur from the HOMO level of C_{60} to that of *a*-IGZO for small back channel/passivation layer gaps. Note that although the *a*-IGZO/none/C_{60} film had the shortest distance between the back channel and C_{60}, the *a*-IGZO/C_8 PA/C_{60} film exhibited additional negative V_{th} shifts due to PA passivation of trap states before C_{60} passivation.[35] A positive V_{th} shift occurred as the alkyl chain length of the PA increased to 12 and 18 *a*-IGZO enhanced the mobility to 2.1 cm^2 V^{-1} s^{-1}, providing high mobility before the deposition of C_{60} to obtain the *a*-IGZO/C_{18} PA/C_{60} device. Therefore, molecular modification of the organic passivation layer *via* alkyl chain length adjustment can be considered to affect not only the passivation of the PBS instability, but also the n-doping of the metal oxide semiconductor.

To verify the proposed doping effect model, we employed a widely used n-type semiconductor, a perylenedicarboximide (PTCDI) derivative with alkyl chain substituents of C1, C8, and C13, as an organic passivation material (Fig. 4a). PTCDI derivatives were selected because their energy levels are similar to those of C_{60} semiconductors, which facilitates electron transfer to the metal oxide semiconducting layer, and the edge-on stacking characteristics of their long-alkyl-chain derivatives are critical for observing the effect of the alkyl chain length.[103] Three types of PTCDI derivatives were vacuum-deposited on

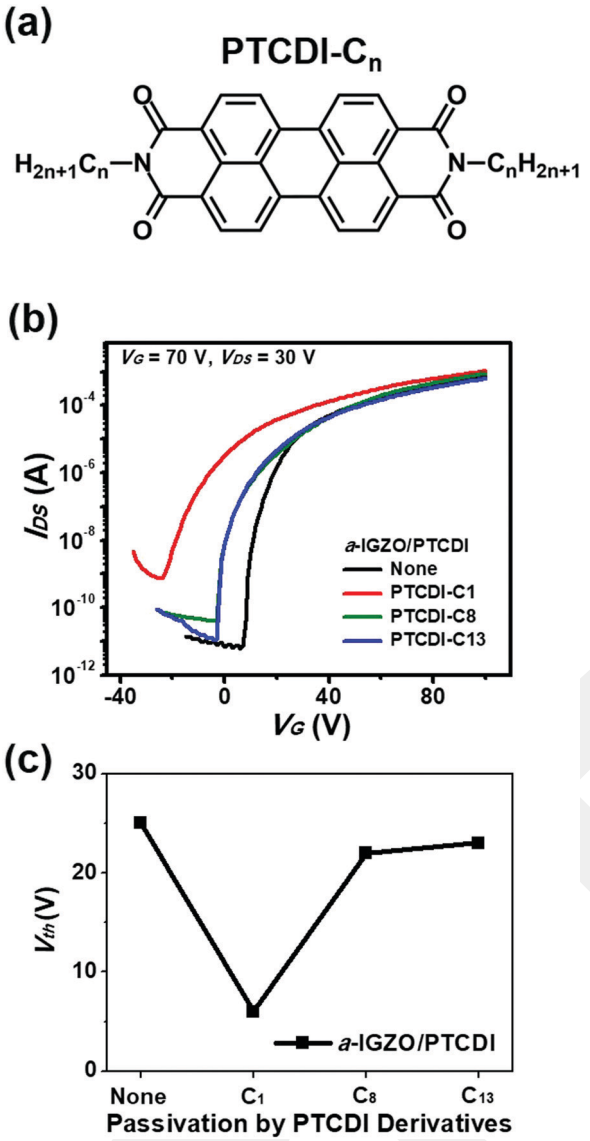

Fig. 4 (a) Molecular structure of PTCDI-C*n*, (b) transfer curves and (c) V_{th} values of the unpassivated and PTCDI-passivated *a*-IGZO TFTs.

a-IGZO TFTs to examine the film crystallography and electrical characteristics. Fig. S6 (ESI†) shows the results of standard θ–2θ XRD scans of the PTCDI-based thin films, which reveal the microstructural order. For thin films of PTCDI-C1, no first-order reflection peaks were observed at $2\theta < 10^{\circ}$, indicating the absence of an edge-on molecular long-axis orientation along the substrate.[104] Instead, multiple diffraction peaks at 2θ = 24.06°, 25.56°, and 27.66° (Fig. S6a, ESI†) were observed, which correspond to *d*-spacings of 3.69, 3.48, and 3.22 Å, respectively. These spacings are much smaller than the calculated long-axis molecular length (~14.7 Å). Because the short molecular axis is calculated to be ~6.62 Å, the observed multiple peaks can be assigned to second-order reflections, where the first-order *d*-spacings (6.44–7.38 Å) are consistent with the short molecular axis. Therefore, it can be assumed that PTCDI-C1 molecules are more likely to align with their short axis along the substrate normal.[105,106] PTCDI-C8 and PTCDI-C13 have calculated molecular lengths of 31.9 and 44.0 Å, with major diffraction peaks at 2θ = 4.38° and 3.32°, which correspond to *d*-spacings of 20.2 and 26.6 Å, respectively (Fig. S6b and c, ESI†). Thus, the two derivatives with longer alkyl chains exhibit a tilted edge-on stacking structure with respect to the substrate plane.[107,108] It is known that the molecular stacking orientation of π-conjugated OSCs indicates the determination of 3D charge transfer direction and affects the charge characteristics.[109] Therefore, different electrical characteristics are expected when PTCDI derivatives with different alkyl chain lengths are applied as passivation materials.

The *I*–*V* curves of the PTCDI-passivated devices were analyzed to examine the initial V_{th} values and determine the n-doping effects. As shown in Table 3 and Fig. 4b, c, the shifts in the V_{th} and mobility values of the PTCDI-passivated devices are similar to those of the PA-modified C_{60}-passivated devices, which validates the n-doping model of organic passivation. Suitable n-doping is realized by PTCDI-C1 passivation, where V_{th} exhibits a significant shift from 25 to 6.0 V, and the mobility is enhanced from 1.1 to 1.5 $cm^2\ V^{-1}\ s^{-1}$. As the alkyl chain length increases to 8 and 13, V_{th} returns to lower values of 22 and 23 V, indicating poor doping characteristics resulting from poor electron transfer from the HOMO level due to the longer alkyl chains. The electron mobility is maintained at 1.5 $cm^2\ V^{-1}\ s^{-1}$ for PTCDI-C8 passivation, whereas it decreases to 1.0 $cm^2\ V^{-1}\ s^{-1}$ for PTCDI-C13 passivation. This result indicates that when an alkyl chain as long as C13 is positioned between the conjugated organic core and the metal oxide semiconductor back channel, most of the n-doping effects of the passivation material are eliminated. Alkyl chain modification of the organic passivation materials significantly affects the doping of metal oxide semiconductors, similar to the effect of alkyl chain modification on the PBS instability. Therefore, an n-doping model of organic passivation materials can also be proposed in conjunction with the PBS instability model of C_{60} passivation by PA monolayers with various alkyl chain lengths, and the model can be verified using PTCDI derivatives.

2.4 Application of the organic passivation model

Finally, we applied the proposed organic passivation model to the discovery of new organic passivation materials. Our model proposes that OSCs with HOMO levels near the Fermi level of the AOSs can be employed as electron-donating defect-passivation materials, which compensate for acceptor-like DOS states in the

Table 3 Representative electrical performance of amorphous IGZO thin-film transistors under different PTCDI derivative passivation conditions.[a] [μ_e: electron mobility ($cm^2\ V^{-1}\ s^{-1}$), V_{th}: threshold voltage (V), I_{on}/I_{off}: current on/off ratio]

	Parameter		
Org. pass.	μ_e ($cm^2\ V^{-1}\ s^{-1}$)	V_{th} (V)	I_{on}/I_{off}
None	1.1	25	1.2×10^8
PTCDI-C1	1.5	6	1.4×10^6
PTCDI-C8	1.5	22	2.2×10^7
PTCDI-C13	1.0	23	5.8×10^7

[a] Measured in vacuum; exhibited n-type characteristics.

subgap, resulting in PBS device stability. HOMO level pinning is known to occur when the ionization energy of the organic material equals the Fermi energy of the AOS, where electron transfer is generated from an organic material with ionization energies that are lower than the metal oxide's work function.[110] Although the ionization energies of the organic materials employed in this study are higher than the *a*-IGZO work function, our previous study demonstrated that such low-LUMO OSCs with ionization energies that are near the metal oxide work function exhibit sufficient electron transfer to fill the subgap states.[43] In addition, the organic passivation materials can induce n-doping effects, which depend on its molecular stacking structure on the oxide surface and can be used to tune the V_{th} values of TFTs. Both passivation effects are degraded as the π-conjugated core of the OSC is separated from the AOS back-channel surface and obstructed by alkyl chains. To explore a wide range of new organic passivation materials according to our proposed organic passivation model, we selected and tested a 4,4-difluoro-4-bora-3*a*,4*a*-diaza-*s*-indacene (BODIPY)-based semiconductor from our previous study.[104] BODIPYs are widely employed for the construction of organic TFTs and organic photovoltaics owing to their highly electron-deficient and coplanar π core with good π-delocalization, a stable LUMO level, and facile synthesis/functionalization at several positions.[111] Here, the n-type BODIPY-based semiconductor BDY-3T-BDY (Fig. 5a) was synthesized according to our previous report and vacuum-deposited on *a*-IGZO TFTs as a passivation layer. The *a*-IGZO TFTs were fabricated using the same method, and PBS tests were applied to observe the device stability. BDY-3T-BDY contains no additional alkyl chains and reportedly has a HOMO level of −5.89 eV, which is lower than that of C_{60} (6.1 eV).[112] In addition, the vacuum-deposited films exhibit amorphous structure in which the π-conjugated core is stacked in random directions; thus, the n-doping effects may be moderate compared to those of film structures with face-on π-conjugated cores.[104] These characteristics make BDY-3T-BDY an appropriate passivation layer candidate, as indicated by the proposed model. Additional θ–2θ XRD scans in Fig. 5b revealed amorphous structure of the vacuum-deposited BDY-3T-BDY films on the *a*-IGZO TFTs, which is consistent with the reported film structure. As shown in Table 4 and Fig. 5c, PBS tests of the passivated *a*-IGZO/BDY-3T-BDY device yielded a ΔV_{th} value of 7 V, which indicates good passivation by BDY-3T-BDY in the absence of PA passivation of the *a*-IGZO back channel. A negatively shifted V_{th} value of 10 V was also observed, indicating n-doping of the *a*-IGZO semiconductor layer by BDY-3T-BDY. Therefore, the proposed organic passivation model was successfully verified by applying BDY-3T-BDY as a passivation layer on *a*-IGZO, and we expect the model to inspire new research supporting future development of organic passivation materials.

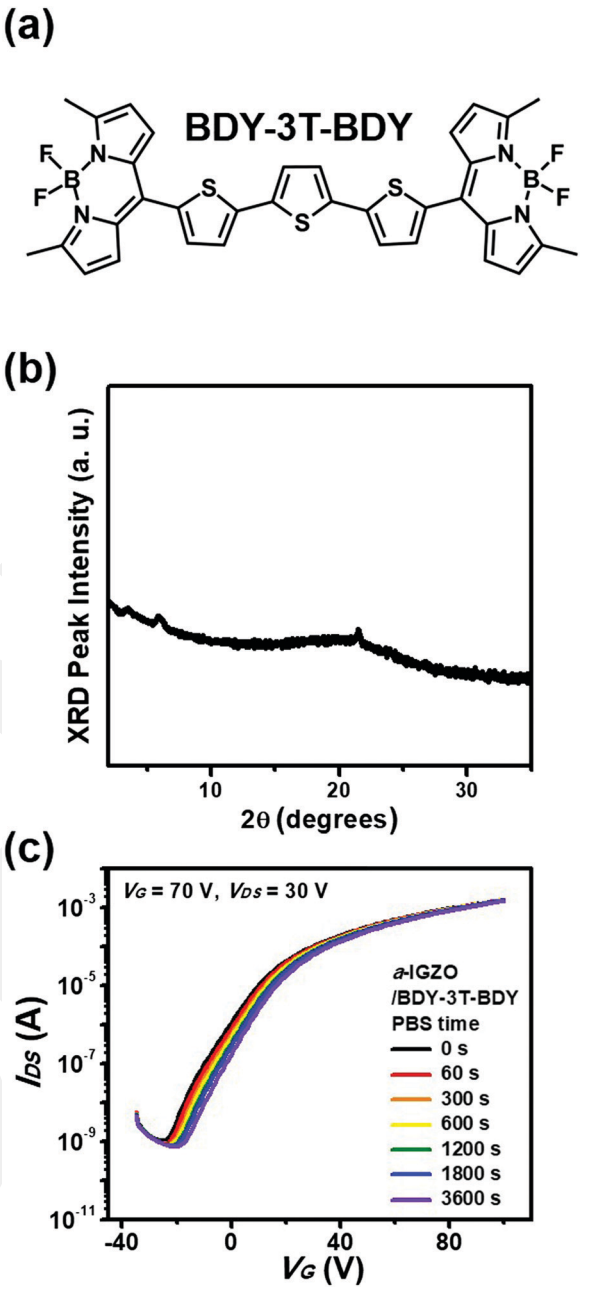

Fig. 5 (a) Molecular structure, (b) XRD pattern, and (c) PBS test results for BDY-3T-BDY-passivated *a*-IGZO TFTs.

3. Conclusion

We investigated the effects of the alkyl chain length of organic passivation materials on *a*-IGZO metal oxide semiconductors. Organic passivation results in PBS-stable TFTs and n-doping of the metal oxide semiconductor; the model was developed using PA monolayers with different alkyl chain lengths to determine their effect in conjunction with that of C_{60} deposition on top of the PA-treated *a*-IGZO back channel. PBS tests of the passivated *a*-IGZO TFTs revealed that the organic passivation originates in the combined effect of both the OSC and the alkyl chain. The unpassivated *a*-IGZO TFT exhibited a ΔV_{th} value of 34 V during PBS; by contrast, the TFT with the optimal C_{12} PA/C_{60} passivation layer had a ΔV_{th} value of 4 V. When the alkyl chain length was further extended to 18 (C_{18} PA/C_{60}), ΔV_{th} increased to 11 V.

Table 4 Representative electrical performance of BDY-3T-BDY-passivated amorphous IGZO thin-film transistors.[a] [μ_e: electron mobility ($cm^2\ V^{-1}\ s^{-1}$), V_{th}: threshold voltage (V), I_{on}/I_{off}: current on/off ratio]

		Positive bias stress							
Org. pass.	Parameter	0	60	300	600	1200	1800	3600	Δ
BDY-3T-BDY	μ_e	1.9	1.9	2.0	2.1	2.2	2.2	2.2	0.3
	V_{th}	10	13	15	15	16	16	17	7
	I_{on}/I_{off}	3.5×10^6	4.6×10^6	5.3×10^6	6.0×10^6	6.1×10^6	6.0×10^6	5.7×10^6	

[a] Measured in vacuum; exhibited n-type characteristics.

Because the PBS stability is attributed to the compensation of dangling bonds in the back channel and reduction of trap states in the channel layer, the alkyl chain length can be considered to affect the overall defect state of the oxide semiconductor layer. Additionally, the optimal passivation condition was expanded to include annealing of the *a*-IGZO TFTs at 390 °C to obtain stable, high-performance *a*-IGZO TFTs, which had an electron mobility and ΔV_{th} of 5.4 $cm^2\ V^{-1}\ s^{-1}$ and 0 V, respectively. In addition, the DOSs of the *a*-IGZO/C_{12} PA/C_{60}, *a*-IGZO (390 °C), and *a*-IGZO (390 °C)/C_{12} PA/C_{60} were determined to confirm the effects of passivation on the subgap defect states. The total DOS values followed the order *a*-IGZO (390 °C)/C_{12} PA/C_{60} < *a*-IGZO (390 °C) < *a*-IGZO/C_{12} PA/C_{60}, which is consistent with the ΔV_{th} results of 0, 2, and 4 V, respectively. Finally, the n-doping characteristics were investigated for the same passivation model, where C_{60} passivation with shorter PA alkyl chain lengths yielded stronger n-doping. The model was verified by the similar n-doping results obtained by passivation by PTCDI derivatives with different alkyl chain lengths, which induced different molecular stacking structures. The short-axis molecular alignment along the substrate normal of short alkyl chains afforded better charge transfer, resulting in stronger n-doping compared to the long-axis molecular alignment orientations of longer alkyl chains. Finally, the BODIPY semiconductor BDY-3T-BDY was synthesized and selected as a passivation material on the basis of our proposed organic passivation model and exhibited good passivation in *a*-IGZO TFTs. This in-depth study of the molecular modification of organic passivation materials and its mechanism suggests that appropriate molecular design of organic materials has strong potential for further development of organic passivation in terms of the electronic stability of metal oxide semiconductors and opens a remarkable platform for molecular engineering of organic passivation materials.

4. Experimental section

4.1 Precursor solution preparation

All the reagents used to prepare the *a*-IGZO solution were purchased from Sigma-Aldrich and used without further purification. A precursor solution with a total metal concentration of 0.2 M was obtained by dissolving indium nitrate hydrate [$In(NO_3)_3{\cdot}xH_2O$, 99.999%], gallium nitrate hydrate [$Ga(NO_3)_3{\cdot}xH_2O$, 99.999%], and zinc nitrate hydrate [$Zn(NO_3)_2{\cdot}xH_2O$, 99.999%] in 2-methoxyethanol (HPLC grade) and stirring the mixture at 70 °C for 2 h and at room temperature for 3 h before use. The molar ratio of In, Ga, and Zn was 6 : 2 : 2.

4.2 *a*-IGZO film preparation and device fabrication

To fabricate *a*-IGZO TFTs, heavily n-doped silicon wafers (n^{++}-Si) were used as gate electrodes, with a thermally grown 300 nm SiO_2 layer as the gate insulator. The SiO_2/Si substrates were cleaned by sonication in Alconox solution (Alconox, Inc.), deionized water, isopropanol, and acetone for 10 min each and dried using N_2 followed by air plasma for 5 min (Harrick Plasma, 18 W). The *a*-IGZO precursor solutions were spin-coated onto the substrates at 4000 rpm for 35 s and then annealed at 310 °C or 390 °C for 30 min in air. The spin-coating and annealing steps were repeated to coat the substrates with two layers. Next, titanium/gold (thickness = 5/40 nm) source/drain (S/D) electrodes with a channel width and length of 2000 and 100 μm, respectively, were deposited on the prepared substrates by thermal evaporation through a shadow mask.

4.3 Fabrication of organic passivation layers

To vary the distance between the oxide semiconductor and C_{60} fullerene molecules (SOL5060; Solaris Chem Inc.), phosphonic acid monolayers with different chain lengths (octylphosphonic acid, dodecylphosphonic acid, and octadecylphosphonic acid, purchased from Alfa Aesar and TCI), were applied on top of the prepared *a*-IGZO TFTs. The devices were immersed in a solution of ethanol and 1 mM phosphonic acid for 5 h at 60 °C and then rinsed with ethanol and dried using N_2. C_{60} powder was vacuum-deposited on top of the devices at a chamber pressure of 3.2×10^{-7} Torr and a deposition rate of 0.1 Å s^{-1}.

N,*N*′-Dimethyl-3,4,9,10-perylenetetracarboxylic diimide, *N*,*N*′-di-*n*-octyl-3,4,9,10-perylenetetracarboxylic diimide, and *N*,*N*′-ditridecyl-3,4,9,10-perylenetetracarboxylic diimide were purchased from TCI and vacuum-deposited on the *a*-IGZO TFTs. The PTCDI derivatives were deposited at a rate of 0.1 Å s^{-1} and a chamber pressure of 3.2×10^{-7} Torr.

BDY-3T-BDY was synthesized following a previously reported procedure[104] and deposited on the *a*-IGZO TFTs at a rate of 0.1 Å s^{-1} and a chamber pressure of 3.2×10^{-7} Torr.

4.4 Device fabrication and characterization

The current–voltage characteristics of the fabricated TFTs were measured using a Keithley 4200 SCS under vacuum conditions. The carrier mobility (μ) was calculated in the saturation regime using the formula

$$\mu_{sat} = (2I_{DS}L)/[WC_i(V_G - V_{th})^2],$$

where I_{DS} is the S/D current, L is the channel length, W is the channel width, C_i is the areal capacitance of the gate dielectric, and V_G is the gate voltage. The surface morphology was characterized using an atomic force microscope (NX10, Park Systems), and the film microstructure was measured by XRD (Ultima IV, Rigaku). The X-ray photoemission scans were conducted using a K-alpha+ instrument (Thermo Fisher Scientific) with an Al Kα source at 1486.6 eV and a base pressure of 7.83×10^{-9} mbar. The adventitious C 1*s* peak at 284.8 eV was employed as a reference to calibrate the binding energies. After a linear baseline was subtracted, three Gaussian–Lorentzian product peak functions were used to fit the O 1*s* spectra. The peak shape, width, and amplitude coefficients were employed as the fitting parameters, where the peak positions were fixed within a certain range according to the typical binding energy of the material. Finally, the areas of the deconvoluted peaks were calculated. The DOSs were obtained using the unified subthreshold coupling factor technique,[88] which allows robust determination of the subgap DOS in amorphous TFTs.

Conflicts of interest

There are no conflicts to declare.

Acknowledgements

This work was supported by National Research Foundation of Korea (NRF) grants funded by the Korean government (No. 2020R1C1C1003606, 2017M2B2A9A02049820, 2020R1A2C4001617, 2018R1A4A1022647).

References

1 T. Durkop, S. A. Getty, E. Cobas and M. S. Fuhrer, *Nano Lett.*, 2004, **4**, 35.
2 Y.-H. Kim, J.-S. Heo, T.-H. Kim, S. Park, M.-H. Yoon, J. Kim, M. S. Oh, G.-R. Yi, Y.-Y. Noh and S. K. Park, *Nature*, 2012, **489**, 128.
3 J. Liu, H. Zhang, H. Dong, L. Meng, L. Jiang, L. Jiang, Y. Wang, J. Yu, Y. Sun, W. Hu and A. J. Heeger, *Nat. Commun.*, 2015, **6**, 10032.
4 H.-J. Yun, S.-J. Kang, Y. Xu, S. O. Kim, Y.-H. Kim, Y.-Y. Noh and S.-K. Kwon, *Adv. Mater.*, 2014, **26**, 7300.
5 H. Yabuta, M. Sano, K. Abe, T. Aiba, T. Den, H. Kumomi, K. Nomura, T. Kamiya and H. Hosono, *Appl. Phys. Lett.*, 2006, **89**, 112123.
6 N. Gong, C. Park, J. Lee, I. Jeong, H. Han, J. Hwang, J. Park, K. Park, H. Jeong, Y. Ha and Y. Hwang, *SID Int. Symp. Dig. Tech. Pap.*, 2012, **43**, 784.
7 S. Jeong, Y.-G. Ha, J. Moon, A. Facchetti and T. J. Marks, *Adv. Mater.*, 2010, **22**, 1346.
8 J. Y. Kwon, K. S. Son, J. S. Jung, T. S. Kim, M. K. Ryu, K. B. Park, B. W. Yoo, J. W. Kim, Y. G. Lee, K. C. Park, S. Y. Lee and J. M. Kim, *IEEE Electron Device Lett.*, 2008, **29**, 1309.
9 J. K. Jeong, *J. Mater. Res.*, 2013, **28**, 2071.
10 E. Fortunato, P. Barquinha and R. Martins, *Adv. Mater.*, 2012, **24**, 2945.
11 S. H. Cho, M. K. Ryu, H.-O. Kim, O.-S. Kwon, E.-S. Park, Y.-S. Roh, C.-S. Hwang and S.-H. Ko Park, *Phys. Status Solidi A*, 2016, **211**, 2126.
12 B. Park, D. Ho, G. Kwon, S. Y. Seo, C. Kim and M. G. Kim, *Adv. Funct. Mater.*, 2018, **28**, 1802717.
13 M.-H. Kim, Y.-S. Ko, H.-S. Choi, S.-M. Ryu, S.-H. Jeon, J.-H. Jung and D.-K. Choi, *Phys. Status Solidi A*, 2016, **213**, 1873.
14 Y.-J. Cho, W.-S. Kim, Y.-H. Lee, J. Park, G. Kim and O. Kim, *Solid-State Electron.*, 2018, **144**, 95.
15 K. H. Ji, J.-I. Kim, H. Y. Jung, S. Y. Park, R. Choi, U. K. Kim, C. S. Hwang, D. Lee, H. Hwang and J. K. Jeong, *Appl. Phys. Lett.*, 2011, **98**, 103509.
16 H.-K. Noh, K. J. Chang, B. Ryu and W.-J. Lee, *Phys. Rev. B: Condens. Matter Mater. Phys.*, 2011, **84**, 115205.
17 D. K. Seo, S. Shin, H. H. Cho, B. H. Kong, D. M. Whang and H. K. Cho, *Acta Mater.*, 2011, **59**, 6743.
18 R. A. Street, T. N. Ng, R. A. Lujan, I. Son, M. Smith, S. Kim, T. Lee, Y. Moon and S. Cho, *ACS Appl. Mater. Interfaces*, 2014, **6**, 4428.
19 S. Choi, J. Jang, H. Kang, J. H. Baeck, J. U. Bae, K. S. Park, S. Y. Yoon, I. B. Kang, D. M. Kim, S. J. Choi, Y. S. Kim, S. Oh and D. H. Kim, *IEEE Electron Device Lett.*, 2017, **38**, 580.
20 P.-T. Liu, C.-H. Chang and C.-J. Chang, *Appl. Phys. Lett.*, 2016, **108**, 261603.
21 Y. Jeong, C. Bae, D. Kim, K. Song, K. Woo, H. Shin, G. Cao and J. Moon, *ACS Appl. Mater. Interfaces*, 2010, **2**, 611.
22 E. Chong, K. C. Jo and S. Y. Lee, *Appl. Phys. Lett.*, 2010, **96**, 152102.
23 H.-H. Nahm and Y.-S. Kim, *NPG Asia Mater.*, 2014, **6**, e143.
24 M. Fakhri, H. Johann, P. Gorrn and T. Riedl, *ACS Appl. Mater. Interfaces*, 2012, **4**, 4453.
25 D. Kim, S. Yoon, Y. Jeong, Y. Kim and M. Hong, *Appl. Phys. Express*, 2012, **5**, 021101.
26 Y.-C. Chen, T.-C. Chang, H.-W. Li, W.-F. Chung, C.-P. Wu, S.-C. Chen, J. Lu, Y.-H. Chen and Y.-H. Tai, *Appl. Phys. Lett.*, 2012, **100**, 262908.
27 M. D. H. Chowdhury, M. Mativenga, J. G. Um, R. K. Mruthyunjaya, G. N. Heiler, T. J. Tredwell and J. Jang, *IEEE Trans. Electron Devices*, 2015, **62**, 869.
28 S.-Y. Huang, T.-C. Chang, M.-C. Chen, S.-C. Chen, C.-T. Tsai, M.-C. Hung, C.-H. Yu, C.-H. Chen, J.-J. Chang and W.-L. Liau, *Electrochem. Solid-State Lett.*, 2011, **14**, H177.
29 J. Wu, Y. Chen, D. Zhou, Z. Hu, H. Xie and C. Dong, *Mater. Sci. Semicond. Process.*, 2015, **29**, 277.
30 D.-S. Han, J.-H. Park, M.-S. Kang, S.-R. Shin, Y.-J. Jung, D.-K. Choi and J.-W. Park, *J. Electron. Mater.*, 2015, **44**, 651.
31 C. Dong, J. Shi, J. Wu, Y. Chen, D. Zhou, Z. Hu, H. Xie, R. Zhan and Z. Zou, *Mater. Sci. Semicond. Process.*, 2014, **20**, 7.
32 S.-J. Seo, S. Yang, J.-H. Ko and B.-S. Bae, *Electrochem. Solid-State Lett.*, 2011, **14**, H375.
33 W. Xu, D. Liu, H. Wang, L. Ye, Q. Miao and J.-B. Xu, *Appl. Phys. Lett.*, 2014, **104**, 173504.

34 M. S. Rajachidambaram, A. Pandey, S. Vilayurganapathy, P. Nachimuthu, S. Thevuthasan and G. S. Herman, *Appl. Phys. Lett.*, 2013, **103**, 171602.
35 P. Xiao, L. Lana, T. Dong, Z. Lin, W. Shi, R. Yao, X. Zhu and J. Peng, *Appl. Phys. Lett.*, 2014, **104**, 051607.
36 S.-H. Cho, Y.-U. Lee, J.-S. Lee, K.-M. Jo, B. S. Kim, H.-S. Kong, J.-Y. Kwon and M.-K. Han, *J. Disp. Technol.*, 2012, **8**, 1.
37 K. H. Kim, Y.-H. Kim, H. J. Kim, J.-I. Han and S. K. Park, *IEEE Electron Device Lett.*, 2011, **32**, 524.
38 S.-H. Choi, J.-H. Jang, J.-J. Kim and M.-K. Han, *IEEE Electron Device Lett.*, 2012, **33**, 381.
39 X. Xu, L. Feng, S. He, Y. Jin and X. Guo, *IEEE Electron Device Lett.*, 2012, **33**, 1420.
40 A. Olziersky, P. Barquinha, A. Vila, L. Pereira, G. Goncalves, E. Fortunato, R. Matins and J. R. Morante, *J. Appl. Phys.*, 2010, **108**, 064505.
41 K. Y. Shin, Y. J. Tak, W.-G. Kim, S. Hong and H. J. Kim, *ACS Appl. Mater. Interfaces*, 2017, **9**, 13278.
42 H. Yoo, Y. J. Tak, W.-G. Kim, Y.-G. Kim and H. J. Kim, *J. Mater. Chem. C*, 2018, **6**, 6187.
43 G. Kwon, K.-T. Kim, B. D. Choi, C. H. Lee, Y.-Y. Noh, S. Y. Seo, C. Kim and M.-G. Kim, *Adv. Mater.*, 2017, **29**, 1607055.
44 D. Ho, H. Jeong, S. Choi and C. Kim, *J. Mater. Chem. C*, 2020, DOI: 10.1039/D0TC02379E.
45 Z. B. Henson, K. Müllen and G. C. Bazan, *Nat. Chem.*, 2012, **4**, 699.
46 D. Ho, S. Vegiraju, D. Choi, J.-R. Yu, G. Kwon, C. Kim and M.-C. Chen, *Dyes Pigm.*, 2019, **163**, 725.
47 Z. Ma, H. Geng, D. Wang and Z. Shuai, *J. Mater. Chem. C*, 2016, **4**, 4546.
48 Y. D. Park, D. H. Kim, Y. Jang, J. Cho, M. Hwang, H. S. Lee, J. A. Lim and K. Cho, *Org. Electron.*, 2006, **7**, 514.
49 M. Al-Hussein, H. C. Hesse, J. Weickert, L. Dössel, X. Feng, K. Müllen and L. Schmidt-Mende, *Thin Solid Films*, 2011, **520**, 307.
50 J. Nelson, J. J. Kwiatkowski, J. Kirkpatrick and J. M. Frost, *Acc. Chem. Res.*, 2009, **42**, 1768.
51 C. Duan, R. E. M. Willems, J. J. van Franeker, B. J. Bruijnaers, M. M. Wienk and R. A. J. Janssen, *J. Mater. Chem. A*, 2016, **4**, 1855.
52 K. Ide, K. Nomura, H. Hosono and T. Kamiya, *Phys. Status Solidi A*, 2019, **216**, 1800372.
53 M. Kimura, T. Nakanishi, K. Nomura, T. Kamiya and H. Hosono, *Appl. Phys. Lett.*, 2008, **92**, 133512.
54 K. Hoshino, D. Hong, H. Q. Chiang and J. F. Wager, *IEEE Trans. Electron Devices*, 2009, **56**, 1365.
55 G.-W. Chang, T.-C. Chang, Y.-E. Syu, T.-M. Tsai, K.-C. Chang, C.-H. Tu, F.-Y. Jian, Y.-C. Hung and Y.-H. Tai, *Thin Solid Films*, 2011, **520**, 1608.
56 K. Itaka, M. Yamashiro, J. Yamaguchi, M. Haemori, S. Yaginuma, Y. Matsumoto, M. Kondo and H. Koinuma, *Adv. Mater.*, 2006, **18**, 1713.
57 P. Xiao, L. Lan, T. Dong, Z. Lin, S. Sun, W. Song and J. Peng, *IEEE Electron Device Lett.*, 2015, **36**, 687.
58 C. Donley, D. Dunphy, D. Paine, C. Carter, K. Nebesny, P. Lee, D. Alloway and N. R. Armstrong, *Langmuir*, 2002, **18**, 450.
59 P.-T. Hsieh, Y.-C. Chen, K.-S. Kao and C.-M. Wang, *Appl. Phys. A: Mater. Sci. Process.*, 2008, **90**, 317.
60 C. L. Perkins, *J. Phys. Chem. C*, 2009, **113**, 18276.
61 P. J. Hotchkiss, M. Malicki, A. J. Giordano, N. R. Armstrong and S. R. Mader, *J. Mater. Chem.*, 2011, **21**, 3107.
62 P. J. Hotchkiss, S. C. Jones, S. A. Paniagua, A. Sharma, B. Kippelen, N. R. Armstrong and S. R. Marder, *Acc. Chem. Res.*, 2012, **45**, 337.
63 P. B. Paramonov, S. A. Paniagua, P. J. Hotchkiss, S. C. Jones, N. R. Armstrong, S. R. Marder and J. L. Bredas, *Chem. Mater.*, 2008, **20**, 5131.
64 X. Du, B. T. Flynn, J. R. Motley, W. F. Stickle, H. Bluhm and G. S. Herman, *ECS J. Solid State Sci. Technol.*, 2014, **3**, Q3045.
65 D. Erbahar, T. Susi, X. Rocquefelte, C. Bittencourt, M. Scardamaglia, P. Blaha, P. Guttmann, G. Rotas, N. Tagmatarchis, X. Zhu, A. P. Hitchcock and C. P. Ewels, *Sci. Rep.*, 2016, **6**, 35605.
66 J. Onoe, K. Takeuchi, K. Ohno and Y. Kawazoe, *J. Vac. Sci. Technol., A*, 1998, **16**, 385.
67 Y. Yamakoshi, N. Umezawa, A. Ryu, K. Arakane, N. Miyata, Y. Goda, T. Masumizu and T. Nagano, *J. Am. Chem. Soc.*, 2003, **125**, 12803.
68 R. B. M. Cross and M. M. De Souza, *Appl. Phys. Lett.*, 2006, **89**, 263513.
69 Y. Vygranenko, K. Wang and A. Nathan, *Appl. Phys. Lett.*, 2007, **91**, 263508.
70 K. Nomura, T. Kamiya, M. Hirano and H. Hosono, *Appl. Phys. Lett.*, 2009, **95**, 013502.
71 A. Suresh and J. Muth, *Appl. Phys. Lett.*, 2008, **92**, 033502.
72 S. Park, C.-H. Kim, W.-J. Lee, S. Sung and M.-H. Yoon, *Mater. Sci. Eng., R*, 2017, **114**, 1.
73 S. Hwang, J. H. Lee, C. H. Woo, J. Y. Lee and H. K. Cho, *Thin Solid Films*, 2011, **519**, 5146.
74 C.-H. Tu, W.-T. Lin, C.-H. Chen, M.-C. Hung, J.-J. Chang, M.-F. Chiang and W.-l. Liao, *SID Int. Symp. Dig. Tech. Pap.*, 2011, **42**, 1151.
75 S.-Y. Huang, T.-C. Chang, M.-C. Chen, S.-W. Tsao, S.-C. Chen, C.-T. Tsai and H.-P. Lo, *Solid-State Electron.*, 2011, **61**, 96.
76 L. Zeininger, L. Portilla, M. Halik and A. Hirsch, *Chem. – Eur. J.*, 2016, **22**, 13506.
77 S. P. Pujari, L. Scheres, A. T. M. Marcelis and H. Zuilhof, *Angew. Chem. Int. Ed.*, 2014, **53**, 6322.
78 E. Jiang, Y. Ai, J. Yan, N. Li, L. Lin, Z. Wang, C. Shou, B. Yan, Y. Zeng, J. Sheng and J. Ye, *ACS Appl. Mater. Interfaces*, 2019, **11**, 36727.
79 Z. Ye, Y. Yuan, H. Xu, Y. Liu, J. Luo and M. Wong, *IEEE Trans. Electron Devices*, 2017, **64**, 438.
80 W. Li, L. Li, F. Wang, L. Zheng, J. Xia, F. Qin, X. Wang, Y. Li, R. Liu, D. Wang, Y. Pan and F. Yang, *Chin. Phys. B*, 2017, **26**, 037104.
81 W. H. Han and K. J. Chang, *Phys. Rev. Appl.*, 2016, **6**, 044011.

82 K. Nomura, T. Kamiya, E. Ikenaga, H. Yanagi, K. Kobayashi and H. Hosono, *J. Appl. Phys.*, 2011, **109**, 073726.
83 K. Nomura, T. Kamiya and H. Hosono, *Appl. Phys. Lett.*, 2011, **99**, 053505.
84 J. S. Heo, J. W. Jo, J. Kang, C. Y. Jeong, H. Y. Jeong, S. K. Kim, K. Kim, H. I. Kwon, J. Kim, Y. H. Kim, M. G. Kim and S. K. Park, *ACS Appl. Mater. Interfaces*, 2016, **8**, 10403.
85 W. L. Kalb and B. Batlogg, *Phys. Rev. B: Condens. Matter Mater. Phys.*, 2010, **81**, 035327.
86 C.-Y. Jeong, H.-J. Kim, K. I. Kim, J.-H. Lee and H.-I. Kwon, *J. Vac. Sci. Technol., B*, 2016, **34**, 060601.
87 X. Zhou, Y. Shao, L. Zhang, H. Lu, H. He, D. Han, Y. Wang and S. Zhang, *IEEE Electron Device Lett.*, 2017, **38**, 1252.
88 S. Lee, S. Park, S. Kim, Y. Jeon, K. Jeon, J.-H. Park, J. Park, I. Song, C. J. Kim, Y. Park, D. M. Kim and D. H. Kim, *IEEE Electron Device Lett.*, 2010, **31**, 231.
89 C. Chen, K. Abe, H. Kumomi and J. Kanicki, *IEEE Trans. Electron Devices*, 2009, **56**, 1177.
90 J. Jeong, J. K. Jeong, J.-S. Park, Y.-G. Mo and Y. Hong, *Jpn. J. Appl. Phys.*, 2010, **49**, 03CB02.
91 H. Im, H. Song, J. Park, Y. Hong, J. Ha, S.-B. Ji, J. Jeong and Y. Hong, *IEEE Trans. Electron Devices*, 2017, **64**, 1683.
92 C. E. Kim, E. N. Cho, P. Moon, G. H. Kim, D. L. Kim, H. J. Kim and I. Yun, *IEEE Electron Device Lett.*, 2010, **31**, 1131.
93 Y.-G. Chang, D.-H. Kim, G. Ko, K. Lee, J. H. Kim and S. Im, *IEEE Electron Device Lett.*, 2011, **32**, 336.
94 H.-H. Hsieh, T. Kamiya, K. Nomura, H. Hosono and C.-C. Wu, *Appl. Phys. Lett.*, 2008, **92**, 133503.
95 S. Jun, C. Jo, H. Bae, H. Choi, D. H. Kim and D. M. Kim, *IEEE Electron Device Lett.*, 2013, **34**, 641.
96 T. Kamiya and H. Hosono, *NPG Asia Mater.*, 2010, **2**, 15.
97 H. W. Zan, W. W. Tsai, C. H. Chen and C. C. Tsai, *Adv. Mater.*, 2011, **23**, 4237.
98 N. J. Zhou, M.-G. Kim, S. Loser, J. Smith, H. Yoshida, X. G. Guo, C. Song, H. Jin, Z. H. Chen, S. M. Yoon, A. J. Freeman, R. P. H. Chang, A. Facchetti and T. J. Marks, *Proc. Natl. Acad. Sci. U. S. A.*, 2015, **112**, 7897.
99 S. P. Schiessl, H. Faber, Y. H. Lin, S. Rossbauer, Q. X. Wang, K. Zhao, A. Amassian, J. Zaumseil and T. D. Anthopoulos, *Adv. Mater.*, 2016, **28**, 3952.
100 C. R. Kagan, D. B. Mitzi and C. D. Dimitrakopoulos, *Science*, 1999, **286**, 945.
101 H. B. Wang, Z. T. Liu, M. F. Lo, T. W. Ng, C. S. Lee, D. H. Yan and S. T. Lee, *J. Appl. Phys.*, 2010, **107**, 024510.
102 M. N. Le, H. Kim, Y. K. Kang, Y. Song, X. Guo, Y.-G. Ha, C. Kim and M.-G. Kim, *J. Mater. Chem. C*, 2019, **7**, 10635.
103 C.-H. Kim and I. Kymissis, *J. Mater. Chem. C*, 2017, **5**, 4598.
104 M. Ozdemir, D. Choi, G. Kwon, Y. Zorlu, B. Cosut, H. Kim, A. Facchetti, C. Kim and H. Usta, *ACS Appl. Mater. Interfaces*, 2016, **8**, 14077.
105 H. Yanagi, Y. Toda and T. Noguchi, *Jpn. J. Appl. Phys.*, 1995, **34**, 3808.
106 A. J. Ferguson and T. S. Jones, *J. Phys. Chem. B*, 2006, **110**, 6891.
107 M. Y. Ameen, T. Abhijith, S. De, S. K. Ray and V. S. Reddy, *Org. Electron.*, 2013, **14**, 554.
108 S. Tatemichi, M. Ichikawa, T. Koyama and Y. Taniguchi, *Appl. Phys. Lett.*, 2006, **89**, 112108.
109 D. H. Kim, Y. D. Park, Y. Jang, H. Yang, Y. H. Kim, J. I. Han, D. G. Moon, S. Park, T. Chang, C. Chang, M. Joo, C. Y. Ryu and K. Cho, *Adv. Funct. Mater.*, 2005, **15**, 77.
110 M. T. Greiner, M. G. Helander, W.-M. Tang, Z.-B. Wang, J. Qiu and Z.-H. Lu, *Nat. Mater.*, 2012, **11**, 76.
111 D. Ho, R. Ozdemir, H. Kim, H. Usta and C. Kim, *ChemPlusChem*, 2019, **84**, 18.
112 P. M. Allemand, A. Koch, F. Wudl, Y. Rubin, F. Diederich, M. M. Alvarez, S. J. Anz and R. L. Whetten, *J. Am. Chem. Soc.*, 1991, **113**, 1050.

